

# Homoclinic Bifurcations in the Quasi-Geostrophic Double-Gyre Circulation

**Eric Simonnet**<sup>1</sup>

*Institut Non Linéaire de Nice, Nice, France*

**Michael Ghil**

*Département Terre-Atmosphère-Océan, Ecole Normale Supérieure, Paris, France*

*and*

*Institute of Geophysics and Planetary Physics*

*University of California, Los Angeles, USA*

**Henk Dijkstra**

*Institute for Marine and Atmospheric Research*

*Utrecht University, Utrecht, The Netherlands*

*and*

*Department of Atmospheric Science*

*Colorado State University, Fort Collins, USA*

**February 4, 2005**

*J. Mar. Res., sub judice*

<sup>1</sup>Corresponding author

Institut Non Linéaire de Nice (INLN), UMR 6618 CNRS

1361, route des Lucioles 06560 Valbonne - France

email: eric.simonnet@inln.cnrs.fr

## Abstract

The wind-driven double-gyre circulation in a rectangular basin goes through several dynamical regimes as the amount of lateral friction is decreased. This paper studies the transition to irregular flow in the double-gyre circulation by applying dynamical systems methodology to a quasi-geostrophic, equivalent-barotropic model with a 10-km resolution.

The origin of the irregularities, in space and time, is the occurrence of homoclinic bifurcations that involve phase-space behavior far from stationary solutions. The connection between these homoclinic bifurcations and earlier transitions, which occur at larger lateral friction, is explained. The earlier transitions, such as pitchfork and asymmetric Hopf bifurcation, only involve the nonlinear saturation of linear instabilities, while the homoclinic bifurcations are associated with genuinely nonlinear behavior. The sequence of bifurcations — pitchfork, Hopf, and homoclinic — is independent of the lateral friction and may be described as the unfolding of a singularity that occurs in the frictionless, Hamiltonian limit of the governing equations.

Two distinct chaotic regimes are identified: Lorenz chaos at relatively large lateral friction versus Shilnikov chaos at relatively small lateral friction. Both types of homoclinic bifurcations induce chaotic behavior of the recirculation gyres that is dominated by relaxation oscillations with a well-defined period.

The relevance of these results to the mid-latitude oceans' observed low-frequency variations is discussed. A previously documented 7-yr peak in observed North-Atlantic variability is shown to exist across a hierarchy of models that share the gyre modes and homoclinic bifurcations discussed herein.

# 1. Introduction and motivation

The major motivation behind this theoretical study is to understand the low-frequency variability observed in mid-latitude sea surface temperatures (SSTs) and in particular in the Gulf Stream region. There is now growing evidence that interannual peaks emerge above the red-noise spectrum in these observations. For example, a 7–8-yr peak in North Atlantic variability (Plaut et al. 1995; Moron et al. 1998; Wunsch 1999; Joyce et al. 2000; Da Costa and Colin de Verdière 2002) has been observed in both SST and sea level pressure (SLP) data. Da Costa and Colin de Verdière (2002) state that this observed peak seems to be related, at high latitudes, to a ‘mechanism local to the western boundary wave guide’, whose ‘origin is unclear at the present time.’ A potential origin of this variability is internal to the ocean and appears to take the form of relaxation oscillations of the Gulf Stream downstream of Cape Hatteras.

The low-frequency behavior of the mid-latitude oceans’ wind-driven, double-gyre circulation has attracted considerable attention since the mid-1990s. The study of the steady wind-driven circulation has a long-standing tradition in physical oceanography and can be traced back to the work of Stommel (1948), Munk (1950), and Fofonoff (1954). Veronis (1963, 1966) pioneered the study of the low-frequency variability of the wind-driven ocean circulation, but it is only recently that concepts of dynamical systems theory have been used intensively to understand its physics in greater detail. These concepts have helped understand results in various models of the double-gyre circulation, from the simplest quasi-geostrophic (QG) ones (Cessi and Ierley 1995; Dijkstra and Katsman 1997; Primeau 2002; Ghil et al. 2002a) to single- and multi-layer shallow-water (SW) models (Jiang et al. 1995, JJG hereafter; Speich et al., 1995; Simonnet et al. 1998; Dijkstra and Molemaker 1999; Nauw and Dijkstra 2001; Simonnet et al. 2003a,b).

The first noticeable success using these ideas was achieved by Jiang et al. (1993) and JJG, followed shortly by Cessi and Ierley (1995). In particular, these authors showed that multiple equilibria occur in the double-gyre circulation in a rectangular basin through

symmetry-breaking pitchfork bifurcations. In QG models of the double-gyre circulation in a rectangular basin, there is an internal reflection symmetry when the flow is forced by a symmetric profile of the zonal wind stress. In all generality, systems that possess this symmetry break it as more energy is injected into them. For example, such a pitchfork bifurcation occurs in the one-dimensional dynamical system

$$\dot{x} = x(\mu - x^2),$$

where  $x$  is the state of the system and  $\mu$  a control parameter (see Guckenheimer and Holmes 1990; Chossat and Lauterbach 2000).

For the double-gyre circulation, the unique antisymmetric steady state, with two gyres of equal intensity, transfers its stability to a pair of asymmetric solutions that are mirror images of each other. One of these asymmetric solutions has a more intense subpolar recirculation cell, so that the detached jet is oriented northeastward when leaving the western boundary, while the other asymmetric solution corresponds to the mirror version of the former, with a more intense subtropical recirculation cell and a jet oriented southeastward.

Although the North-Atlantic and North-Pacific surface flows are not that close to possessing such a symmetry, it is still quite useful to study the idealized system of the symmetric double-gyre flow using dynamical system theory. For example, in the symmetric system one can easily determine the branches of steady states since these are connected through pitchfork bifurcations. When the symmetry is no longer exact, for example, due to the presence of continental boundaries, the effect of external asymmetries on the dynamics of the flow can be exactly determined. Such is also the case in SW models of the double-gyre flow, where symmetry is perturbed due to the slight north–south slope of the thermocline: the pitchfork bifurcation observed in symmetric QG models becomes an imperfect pitchfork in SW models (JJG; Dijkstra 2000; Dijkstra and Ghil, 2005).

JJG provided a preliminary description of the bifurcation tree, all the way to aperiodic solutions, but they focused mainly on the first, perturbed-pitchfork bifurcation.

Their results stimulated many complementary studies that examined carefully oscillatory instabilities of the asymmetric steady solutions and their subsequent aperiodic behavior. Resonant Rossby basin modes were studied in the context of the single-gyre case by Sheremet et al. (1997) and in the double-gyre case by Dijkstra and Katsman (1997). These modes play an important role in the variability of the double-gyre circulation (Berloff and McWilliams, 1999; Chang et al. 2001), but do not explain in a satisfactory manner the pronounced interannual and interdecadal variability observed in mid-latitude ocean basins (Yoshida 1961; Bjerknes 1964; Taft 1972; Mizuno and White 1983; Hanson 1991; Qiu and Joyce 1992; Sutton and Allen 1997; Moron et al. 1998).

In the double-gyre circulation, there exist asymmetric oscillatory modes, called gyre modes (Speich et al. 1995; Dijkstra and Katsman 1997; Chang et al. 2001; Simonnet and Dijkstra 2002), which destabilize the asymmetric steady states. These instabilities are associated with Hopf bifurcations and give rise to time-periodic, low-frequency behavior. These modes are not directly related to Rossby wave propagation; they have interannual periods in barotropic models and in small ocean basins, while their periods are decadal in baroclinic models and in large oceanic basins (Hogg et al., 2005; Simonnet, 2005). The gyre modes induce energetic relaxation oscillations around the asymmetric states.

Simonnet and Dijkstra (2002) have shown that the occurrence of the gyre modes in double-gyre flow is strongly related to that of the symmetry-breaking pitchfork bifurcation. The gyre mode appears through the merging of two purely real eigenmodes; one of these two modes, called the P-mode (P for pitchfork), is responsible for the symmetry-breaking bifurcation off the antisymmetric branch of solutions. Multiple equilibria are essential for the occurrence of these gyre modes. Note that the “gyre modes” of Sheremet et al. (1997) are nonoscillatory; the reason is the absence of the P-mode in single-gyre models, where there is no reflection symmetry.

The gyre modes can explain the interannual and interdecadal variability of the double-gyre flows close to the point where these modes become unstable (Nauw and Dijkstra 2001), but cannot fully explain the irregular behavior of these flows at larger forcing or

smaller lateral friction. For instance, JJG's preliminary results on transition to chaos suggest that the limit cycles associated with the interannual gyre modes undergo period doubling in the 1.5-layer SW model, as well as interacting with a saturated subannual mode, to generate lower-frequency, interdecadal variability.

Meacham's (2000) work marks a turning point in the thinking about the transition to chaos in the double-gyre problem. He suggested that irregular behavior does not emerge through successive local instabilities and their nonlinear saturation and competition (Ruelle and Takens 1971), as in single-gyre models (Berloff and Meacham 1997), but rather through the sudden and global change of phase-space geometry caused by a homoclinic bifurcation. The solutions of the barotropic QG model of Meacham (2000) show certain signatures of such a global bifurcation, although the actual homoclinic orbit could not be detected explicitly. Such a global bifurcation appears more clearly in the QG model of Chang et al. (2001), where transitions between solutions with a jet oriented northeastward and those with a jet oriented southeastward were followed through a fairly broad parameter range. These authors attribute the transitions to a figure-8, symmetric homoclinic orbit associated with the unstable antisymmetric steady state.

Nadiga and Luce (2001) went a step further: they were able to locate precisely a homoclinic bifurcation in the parameter space of a barotropic QG model by systematically performing spectral analysis of model solutions near the bifurcation and they conjectured that it was of so-called Shilnikov (1965) type. They also demonstrated the importance of this dynamical phenomenon in explaining low-frequency variability in double-gyre wind-driven flows. A similar homoclinic bifurcation has also been identified in the 2.5-layer SW model of Simonnet et al. (1998; 2003a,b), where baroclinic instabilities are allowed, although complications arise due to the absence of an exact reflection symmetry. In the same way that pitchfork bifurcations are perturbed in SW models, the symmetric homoclinic orbit obtained in idealized QG models (Chang et al. 2001; Nadiga and Luce 2001) becomes perturbed in SW models.

The present paper focuses on the precise connection between the earlier transitions —

in particular the pitchfork bifurcation and associated gyre modes — and the homoclinic bifurcations, in order to understand the origin of the low-frequency relaxation oscillations and the transition to chaos in the double-gyre flows. We show that it is precisely the oscillations arising from the gyre modes that are responsible for the homoclinic bifurcation and chaotic behavior detected by Meacham (2000), Chang et al. (2001), Nadiga and Luce (2001), and Simonnet et al. (1998, 2003b). These oscillations do not saturate in period and amplitude; instead, they become so vigorous, at small enough lateral friction, that they are able to completely change the direction of the mid-latitude jet. The homoclinic bifurcation is hence associated with transitions between flow states with a strong northeastward- and a strong southeastward-oriented jet. Furthermore, we will show that the presence of the homoclinic bifurcation gives rise to two separate regimes of chaotic behavior, depending on the strength of the lateral friction.

In section 2, we introduce the model and the methodology used. Section 3 contains the results on the origin of the homoclinic orbit and its connection to the earlier, local bifurcations: the symmetry-breaking pitchfork bifurcation and the Hopf bifurcations related to the gyres modes. We also compute the loci of the relevant bifurcations, in a two-dimensional parameter plane spanned by the wind-stress intensity and the lateral friction coefficient, and identify several routes to chaos.

Section 4 discusses the relevance of these results to mid-latitude ocean variability. In particular, data analysis of the Gulf Stream axis position is confronted with the theory of the wind-driven circulation in idealized models. In this confrontation, we pay special attention to the 7–8-yr peak in North-Atlantic variability. Concluding remarks follow in section 5.

## 2. Model and methods

### *a. Model*

We consider a reduced-gravity QG model with an active ocean layer of constant density  $\rho$  and thickness  $D$ , which lies above a motionless layer of density  $\rho + \Delta\rho$ . The flow is

confined to a rectangular basin of dimensions  $L_x \times L_y$  and forced by an idealized zonal wind stress of intensity  $\tau_0$ . Using a characteristic horizontal scale  $L$ , a horizontal velocity scale  $U$ , and a time scale  $L/U$ , the nondimensional equations are

$$(1) \quad \begin{aligned} \partial_t q + J(\psi, q) - r_H \nabla^4 \psi &= -\sigma \sin 2\pi \frac{L}{L_y} y, \\ q &\equiv \nabla^2 \psi - \psi + \beta y; \end{aligned}$$

here  $J$  is the Jacobian, defined as  $J(u, v) = \partial_x u \partial_y v - \partial_y u \partial_x v$ ,  $\psi$  is the geostrophic streamfunction,  $\nabla$  the gradient operator, and  $q$  the potential vorticity. The parameters in (1) are the inverse Reynolds number  $r_H$ , the strength of the planetary vorticity gradient  $\beta$ , and the strength of the wind stress  $\sigma$ . Their expressions are given by

$$(2) \quad r_H = \frac{A_H}{UR_d}; \quad \beta = \frac{\beta_0 R_d^2}{U}; \quad \sigma = \frac{\tau_0 R_d}{\rho_0 D U^2},$$

where  $R_d = (g'D)^{1/2}/f_0$  is the Rossby radius of deformation,  $g' = g\Delta\rho/\rho$  is the reduced gravity, and  $A_H$  is the lateral friction coefficient. The reference values of these parameters and the values of the dimensionless inertial and viscous boundary layer thickness,  $\delta_I = R_d^{-1}(U/\beta_0)^{1/2}$  and  $\delta_M = R_d^{-1}(A_H/\beta_0)^{1/3}$ , are given in Table 1. Free-slip boundary conditions, that is  $\psi = \nabla^2 \psi = 0$ , are imposed on the boundaries of the rectangular domain,  $x = 0, L_x$  and  $y = 0, L_y$ .

Table 1

Equations (1) are invariant under the reflection symmetry given by a group action  $\mathcal{S}$  defined as

$$(3) \quad \mathcal{S}[\psi(x, y)] = -\psi(x, L_y - y).$$

It is easy to see that  $\mathcal{S} \circ \mathcal{S} = I$ , the identity operator. This group action is therefore referred to as a  $\mathbb{Z}_2$ -symmetry, since it behaves like adding 1 modulo 2 in the set  $\{0, 1\}$ .

We use the Arakawa (1966) energy- and enstrophy-conserving scheme on a uniform spatial grid. The spatial resolution for the computations of local and global bifurcations is 10 km. To compute steady branches of solutions and bifurcation points, pseudo-arclength

continuation methods (Keller 1977) are used. The main idea is to introduce an extra parameter which approximates the arclength of the branches of solutions in phase-parameter space, and to perform Newton-Raphson steps to track a particular branch of steady solutions; see also Legras and Ghil (1985), Speich et al. (1995), Primeau (1998), chapter 4 in Dijkstra (2000), and Simonnet et al. (2003a).

We carry out the LU decomposition of the Jacobian matrix obtained at each Newton-Raphson step by applying the unsymmetric-pattern, multifrontal method of Davis and Duff (1997). Linear stability analysis of the steady states is also part-and-parcel of our continuation method. The eigenvalues of the Jacobian matrix that are closest to the imaginary axis are those involved in the local bifurcations; they are computed by a spectral transformation of the generalized eigenvalue problem, combined with the Simultaneous Iteration Technique algorithm (Stewart and Jennings 1981). We refer to Kubiček and Marek (1983) and Dijkstra (2000) for further details.

The time integrations of the model use a third-order Adams-Bashforth temporal scheme (Duran 1999), with a time step of 6 hours and a 15-km spatial resolution. This grid is fine enough to resolve properly the western boundary layers, as well as to capture the nonlinear processes involved in the eastward jet and intense recirculation zone, for all parameter values considered here. The size of the basin is  $L_x = 1000$  km and  $L_y = 2000$  km for both the bifurcation analysis and the simulation results. Speich et al. (1995), Chang et al. (2001), Ghil et al. (2002a), and Simonnet et al. (2003a,b) showed that these domain sizes are quite sufficient to capture the main phenomena of interest.

### **3. Transition to irregular variability**

In the first subsection below, we present the connection between the pitchfork bifurcation, the limit cycles associated with the gyre modes, and the existence of a homoclinic bifurcation. In the next subsection, it is shown that a 4-mode truncated model is the minimal model capturing the sequence of bifurcations in our equivalent-barotropic numerical model. Next, we explore the bifurcation loci in the two-parameter plane spanned by the

wind stress strength and the lateral friction coefficient, and the irregular-flow regimes near the homoclinic bifurcations.

*a. The origin of the homoclinic bifurcation*

For a fixed lateral friction coefficient  $A_H = 300 \text{ m}^2\text{s}^{-1}$ , the schematic bifurcation diagram of the QG model is plotted in Fig. 1. “Schematic” refers here to the superimposed trajectories in the figure that help explain the behavior of the solution. The quantity on the  $x$ -axis is the wind-stress strength  $\sigma$  and that on the  $y$ -axis is a measure of the asymmetry of the solutions,  $\Delta_E$ . The latter is defined as  $\Delta_E \equiv E_p - E_t$ , where  $E_p$  is the potential energy of the subpolar recirculation, that is the integral of  $(1/2)|\psi|^2$  restricted to values  $\psi < 0$ , and  $E_t$  is the potential energy of the subtropical recirculation, corresponding to values  $\psi > 0$ .

**Fig. 1**

For small  $\sigma$ , there is a unique antisymmetric steady state, which is stable (solid blue line in Fig. 1). Hence, for every initial state this antisymmetric state is eventually reached as  $t \rightarrow \infty$ . At a critical value of  $\sigma$ , a pitchfork bifurcation occurs (indicated by  $P$  in Fig. 1) and stable asymmetric solutions appear; they are related by the reflection symmetry  $\mathcal{S}$  of Eq. (3) and thus have values  $\Delta_E$  that are equal and of opposite sign. The antisymmetric solution becomes unstable (dotted line) at  $P$  and it undergoes two further bifurcations, indicated by  $L_1$  and  $L_2$  in Fig. 1. These two bifurcations are of saddle-node type and the two may eventually collide into a cusp catastrophe; this bifurcation structure is a generic feature of barotropic QG models of the double-gyre problem (see Cessi and Ierley 1995; Primeau 1998; Simonnet and Dijkstra 2002). These saddle-node bifurcations are in general followed by a second pitchfork bifurcation (not shown) that leads to the appearance of strongly inertial solutions without western boundary layers. Since  $\Delta_E = 0$  along the entire antisymmetric branch, the turning of the branch cannot be seen in the coordinates chosen for Fig. 1.

The relative smallness of the wind-stress value for this region in parameter space is entirely due to the length scale  $L$  chosen, which is 50 km in this study (see Table 1). As a

matter of fact, wind-stress bifurcation values roughly scale like the length  $L$ . Larger and more realistic values would be obtained in multi-layer models, as well as for larger length scales: the wind stress acts in the present model as a body force on the entire depth of the fluid, while in a multi-layer model the wind stress acts only on the uppermost layer; hence its effect on the whole fluid mass would be much smaller.

On the asymmetric branches, merging of two real modes occurs (indicated by the points  $M'$  and  $M''$ ) and gives rise to oscillatory gyre modes (Simonnet and Dijkstra 2002). These oscillatory modes are damped at first and become unstable at the Hopf bifurcations (indicated by the points  $H'$  and  $H''$ ). The stable periodic orbit close to the Hopf bifurcation off the upper branch (positive  $\Delta_E$ ) is shown as the closed curve labeled **a** in Fig. 2; the limit cycle in question appears there as a plot of  $E_p$  versus  $\Delta_E$ . The limit cycles labeled **b** and **c** in Fig. 2 are for slightly larger values of  $\sigma$ . The limit cycles hence span larger and larger regions of phase space as  $\sigma$  increases (at constant  $A_H$ ). They correspond to relaxation oscillations, as the eastward jet shifts abruptly from a very asymmetric path (large  $\Delta_E$ ) to an almost zonal path (small  $\Delta_E$ ). Moreover, the period of these oscillations increases rapidly but it does not saturate (see the caption of Fig. 2). Limit cycles of the same type also occur off the subtropical branch (with negative  $\Delta_E$ ); they are mirror reflections of those around the subpolar branch and are not plotted in Fig. 2.

Fig. 2

For a critical value  $\sigma = \sigma_{hc}$ , the two mirror-symmetric limit cycles merge into a symmetric homoclinic orbit of infinite period. A trajectory near the homoclinic orbit is labeled **d** in Fig. 2 and has mutually symmetric portions in the region of positive  $\Delta_E$  and negative  $\Delta_E$ , thus crossing the antisymmetric state ( $\Delta_E = 0$ ). The homoclinic orbit is not an artifact of the projected dynamics in Fig. 2: it occurs genuinely in the high-dimensional phase space of the discretized model (1) (not shown). The appearance of the homoclinic orbit is also shown schematically in Fig. 1 as the connection of both limit cycles with the unstable antisymmetric state (indicated by A in Fig. 1).

To study the homoclinic bifurcation in greater detail, we consider next a much simpler,

highly truncated model, which captures the same bifurcation sequence. JJG introduced a potentially useful model that arises through mode truncation see also Dijkstra and Ghil (2005). We used here a simple generalization of this type of model.

*b. Low-order model*

JJG modified the original Veronis (1963) model by adding a western boundary-layer structure to his classical Fourier modes. The barotropic QG equations with a bottom-friction term, instead of the usual lateral friction, are projected onto this basis. In JJG, only the two modes corresponding to the first zonal wave component and the first two meridional harmonics were retained, modified by exponential decay away from the western boundary. The set of two ordinary differential equations (ODEs) obtained in JJG exhibits the pitchfork bifurcation observed in full QG models. This set also exhibits the merging process leading to the gyre mode, as shown by Simonnet and Dijkstra (2002).

Nevertheless, the JJG system of two ODEs exhibits neither supercritical Hopf bifurcations nor homoclinic ones. We thus retain the single  $x$ -wave of JJG but extend the JJG truncation to the four  $y$ -mode basis functions on the square domain  $(0, \pi) \times (0, \pi)$  given by

$$(4) \quad \begin{aligned} \phi_1(x, y) &= e^{-sx} \sin x \sin y, & \phi_2(x, y) &= e^{-sx} \sin x \sin 2y, \\ \phi_3(x, y) &= e^{-sx} \sin x \sin 3y, & \phi_4(x, y) &= e^{-sx} \sin x \sin 4y; \end{aligned}$$

here  $s$  measures the width of the western boundary layer, as in JJG. Adding the two higher meridional modes will allow us to capture the essentials of the homoclinic bifurcation and its roots in the pitchfork and Hopf bifurcations.

We consider the purely barotropic case, that is, with  $q = \nabla^2 \Psi + \beta y$  in (1), expand the streamfunction as  $\psi = \sum_{i=1}^4 A_i(t) \phi_i$ , and compute the quantities  $\int_0^\pi \int_0^\pi [\text{Eq. (1)}] \phi_i dx dy$ .

One obtains the system of four ODEs

$$\begin{aligned}
\dot{A}_1 &= c_1 A_1 A_2 + c_2 A_2 A_3 + c_3 A_3 A_4 - \mu A_1 \\
\dot{A}_2 &= c_4 A_2 A_4 + c_5 A_1 A_3 - c_1 A_1^2 - \mu A_2 + \sigma \\
\dot{A}_3 &= c_6 A_1 A_4 - (c_2 + c_5) A_1 A_2 - \mu A_3 \\
\dot{A}_4 &= -c_4 A_2^2 - (c_3 + c_6) A_1 A_3 - \mu A_4
\end{aligned}
\tag{5}$$

where  $c_i$ ,  $i = 1, \dots, 6$  are positive constants, while  $\mu$  is the bottom-friction parameter and  $\sigma$  the wind-stress strength.

We now investigate the first few bifurcations of this model for the particular value  $\mu = 1$  and the values of the coefficients  $c_i$  as given in Table 2. It suffices, in fact, to consider the case  $\mu = 1$  only, since (5) can be rescaled by taking

$$A_i = \mu A'_i \quad ; \quad t = \frac{t'}{\mu}
\tag{6}$$

and  $\sigma = \mu^2 \sigma'$ . This scaling is possible since the terms associated with the  $\beta$ -effect are absent, as in Veronis (1963) and in JJG's two-mode truncated QG model. As we shall see, the absence of Rossby wave dynamics from this low-order model does not preclude it from capturing the modes essential for low-frequency variability in the double-gyre problem.

For any positive values of the coefficients  $c_i$ , the system (5) undergoes a pitchfork bifurcation as  $\sigma$  increases, which yields multiple equilibria in mirror pairs. This general property of (5) is due to the fact that the determinant of the Jacobian along the branch of antisymmetric fixed points ( $A_1 = A_3 = 0$ ) can be written as a quartic polynomial  $P_4(A_2)$  in  $A_2$ ,

$$P_4(A_2) = c_3 c_4^2 c_6 A_2^4 - c_4 (c_2 c_6 - c_3 (c_2 + c_5)) A_2^3 - c_2 (c_2 + c_5) A_2^2 + c_1 A_2 - 1,$$

where  $A_2$  is a solution of the simpler, cubic equation  $c_4 A_2^3 + A_2 - \sigma = 0$ . The key observation, then, is that  $P_4(A_2)$  always crosses the real axis for  $A_2 > 0$  and all  $c_i > 0$ .

Numerically, one finds real-mode merging along the two asymmetric branches, like in Simonnet and Dijkstra (2002). The damped oscillatory modes generated by this merging

then bifurcate off both branches of asymmetric fixed points (Fig. 3), and this pair of limit cycles grows and finally merges into a figure-eight homoclinic orbit. These limit cycles do correspond to the gyre modes observed in more complex models. The bifurcations shown in Fig. 3 were computed with  $s = 2$  but the bifurcation diagram is quite similar for other values of  $s$  (not shown).

**Fig. 3**

All our attempts to project the QG equations (1) onto three modes only, whether Fourier modes or modified-Fourier ones, failed to reproduce the bifurcation diagram in Fig. 3. This suggests that the minimum number of modes needed to exhibit a homoclinic bifurcation associated with the double-gyre flow pattern is four.

*c. Regime diagram of the full model*

A direct consequence of the rescaling (6) in the truncated model, with  $A_i \simeq \mu$  and  $\sigma \simeq \mu^2$ , is that the paths of all the local bifurcation points in the  $(\mu, \sigma)$  parameter plane are quadratic curves and merge at the origin  $\mu = \sigma = 0$ , where friction and wind stress vanish. This observation motivates us to investigate the loci of the different bifurcations for the full, equivalent-barotropic QG-model.

In Fig. 4, the locus of the pitchfork bifurcation, the saddle-node bifurcation  $L_1$  (Fig. 1) and the homoclinic bifurcation are plotted in the  $(r_H, \sigma)$  plane. The locus of the pitchfork bifurcations (light solid) separates the plane into two regions: below the curve only one equilibrium exists, while above it multiple equilibria (three or more) are present.

The locus of the homoclinic bifurcations (heavy solid) is difficult to compute since an analysis of the linearized Eq. (1) is of no help in detecting the merging of the two mirror-symmetric limit cycles shown in Fig. 2. Many time integrations are necessary, instead, in order to detect this bifurcation with sufficient accuracy. Between the loci of the pitchfork and homoclinic bifurcations, both the locus of the mode merging points  $M$  and of the Hopf bifurcations  $H$  off the asymmetric branches of steady states occur (not shown). Finally, the third, dash-dotted curve represents the locus of saddle-node bifurcations  $L_1$  situated on the antisymmetric branch.

**Fig. 4**

The bifurcation loci become harder and harder to compute as  $r_H \rightarrow 0$ , but all three curves shown in Fig. 4 seem to merge at the origin of the regime diagram,  $r_H = \sigma = 0$ , just as in the truncated model. Numerically, we found a sharp limit of very small lateral viscosity  $r_H = 0.3 \cdot 10^{-3}$ , beyond which the spatial 10-km resolution was no longer sufficient to resolve the western boundary layers. The results at  $r_H = 10^{-3}$  were also checked using a finer, 5-km resolution that yielded the same results.

The nonlinear structure underlying Fig. 4 is infinitely degenerated in the limit of  $r_H \rightarrow 0$ , as there is an infinite number of solutions of the inviscid steady-state form of (1), namely  $J(\psi, q) = 0$ ; see also Ghil et al. (2002a) and further references there. At this point, no theoretical results seem to exist to explain the unfolding scenario apparent in Fig. 4 for the barotropic vorticity equation (1) with rectangular geometry, free-slip boundary conditions, and  $\mathbb{Z}_2$ -symmetry. In the truncated model, we showed analytically that the merging is quadratic and this seems to be also the case for the full model. An obstacle to relating the unfoldings in the two models is the fact that the  $\beta$ -term prevents the straightforward rescaling of Eq. (1), as carried out in the truncated model (5).

#### *d. Distinct types of homoclinic bifurcations*

We now show that, depending on the value of  $r_H$ , different kinds of homoclinic bifurcations occur in the equivalent-barotropic QG-model. Note that the figure-8 homoclinic orbit arises through the two limit cycles touching the branch of unstable antisymmetric solutions, as they merge. Wiggins (1987) shows that the linear stability properties of this unstable antisymmetric state (e.g., state *A* in Fig. 1), together with the symmetry properties of the equations, determine the type of behavior near the homoclinic bifurcation. There are basically two cases when ordering the eigenvalues  $\kappa$  of the linear stability problem in decreasing order of their real parts: (i) the first three  $\kappa$ 's are all real, while the first one is positive ( $\kappa_U > 0$ ) and in absolute value larger than the second eigenvalue ( $\kappa_U > |\kappa_S|$ ,  $\kappa_S < 0$ ); (ii) the first eigenvalue is real and positive ( $\kappa_U > 0$ ), while the following two eigenvalues form a complex conjugate pair with negative real part ( $Re(\kappa_S) < 0$ ).

In both cases, the antisymmetric state is unstable to only one real mode (and hence one direction in phase space), but stable to all others. If the unstable steady state is pictured within a plane in Fig. 5, then the stable directions can be sketched as occurring in that plane and the unstable direction as perpendicular to it. The two different cases are distinguished by how the attraction in the stable directions occurs. In the first case, the homoclinic orbit connects the unstable direction with one of the stable directions (see Fig. 5a). In this case, the behavior of the system is akin to the Lorenz (1963) system. In the second case, the homoclinic orbit, after being ejected along the unstable direction, spirals back in on the unstable fixed point (Fig. 5b here; see also Fig 6.12 in Ghil and Childress 1987). In this case, the system displays Shilnikov-type phenomena; see for example, Nadiga and Luce (2001) for further details on this case.

*Fig. 5*

The real part of the eigenvalues along the unstable antisymmetric branch are plotted as a function of  $r_H$  in Fig. 6. At low viscosity ( $r_H < 3.34 \cdot 10^{-3}$ ), we are in the Shilnikov-type case (case (ii) above): the stable-focus behavior ( $Re(\kappa_S) < 0$ ) corresponds to a symmetric Rossby-basin mode of subannual period. The spatial patterns of the imaginary and real part of the eigenfunction are illustrated in the two lower panels of Fig. 6; they indicate the westward propagation and the basin-wide signature of the mode. For  $r_H > 3.34 \cdot 10^{-3}$ , we are in the Lorenz-type case (case (i) above): the two leading eigenvalues correspond precisely to the two modes involved in the merging that gives rise to the gyre modes, that is the P-mode and L-mode of Simonnet and Dijkstra (2002). The familiar tripole (P-mode) and dipole (L-mode) patterns of the streamfunction can be seen in the two right-most panels of Fig. 6. At  $r_H = 3.34 \cdot 10^{-3}$ , the growth factor of the L-mode becomes larger than that of the Rossby-basin mode, while the unstable direction still corresponds to an instability of the antisymmetric state with respect to the P-mode.

*Fig. 6*

Hence at high lateral friction ( $r_H > 3.34 \cdot 10^{-3}$ , that is  $A_H > 167 \text{ m}^2 \text{ s}^{-1}$ ) Lorenz chaos may occur above the locus of the homoclinic bifurcation in the regime diagram (Fig. 4), but a  $\mathbb{Z}_2$ -symmetry is a further prerequisite (Sparrow 1983). Lorenz (1963) chaos is indeed observed in the neighborhood of the unstable antisymmetric steady state that appears as

the lowermost point on the  $y$ -axis ( $\Delta_E = 0$ ) in Fig. 2 (at  $r_H = 6.0 \cdot 10^{-3}$ ). At small lateral friction, Shilnikov (1965) chaos is expected and the behavior in this case is quite complex. The value of the ratio between the rate of ejection along the unstable manifold and the rate of attraction along the stable manifold, namely  $\delta = -\kappa_S/\kappa_U$ , characterizes different types of Shilnikov chaos: type I for  $1/2 < \delta \ll 1$ , type II for  $1/2 \ll \delta < 1$ , and the type for which  $\delta > 1$ ; Nadiga and Luce (2001) provide additional discussion and illustration of two of these types. Types I and II are characterized by chaos both above and below the locus of the homoclinic bifurcation, without the further need for an exact  $\mathbb{Z}_2$ -symmetry.

One may thus expect the Shilnikov (1965) scenario to be strongly favored in more realistic models, such as SW models with rectangular or irregular geometry, as well as at higher Reynolds numbers  $1/r_H$ . The limit cycles associated with the gyre modes undergo an infinite number of period-doubling and saddle-node bifurcations before even encountering the homoclinic reconnection, as observed for instance in the SW models of JJG or Simonnet et al. (2003b).

## 4. Low-frequency variability in the mid-latitude oceans

Model variability near the homoclinic bifurcation is rich and complicated and a detailed analysis of this behavior in the two-parameter plane  $(\sigma, r_H)$  is presented by Simonnet et al. (2005). We call the physically most relevant regime of variability documented there the quasi-homoclinic regime; it is characterized by relaxation oscillations with pronounced interannual-to-interdecadal variability. Several QG and SW model results (Simonnet et al. 2003b; Nauw et al. 2004) can be shown to possess key features of this quasi-homoclinic regime.

An important feature of the dynamics after the homoclinic bifurcation is the behavior of the periods of the limit cycles associated with the relaxation oscillations of the zonal jet. The period of the gyre modes is given at first by the complex conjugate eigenvalues that characterize the Hopf bifurcation, and then tends to infinity at the homoclinic bifurcation. Beyond the latter bifurcation, as one enters more and more energetic and

nonlinear regimes, it appears that the period quickly decreases from infinity to about twice the period observed at the Hopf bifurcation, due to the fact that the limit cycles become symmetric; see Figs. 1–3 here and Figs. 9 and 15 in Chang et al. (2001). The transition across the homoclinic bifurcation, and the very large periods associated with it, is very sharp (Nadiga and Luce, 2001) so that the likelihood to observe it, as well as unrealistically long periods, is quite small, and the more so for more realistic models. This key feature of behavior near homoclinic bifurcation adds relevance to the “period-doubled” gyre modes in explaining interannual signals in the North-Atlantic (see also Simonnet 2005).

We show in Fig. 7a the spectrum of the kinetic energy in the subpolar gyre of a 2.5-layer SW model, whose domain is a realistic Atlantic basin with continental boundaries and whose horizontal resolution is 12 km (see Simonnet et al. 2003b). The solution whose spectrum is shown is conjectured to lie in the quasi-homoclinic regime above.

The spectral results shown in Fig. 7a, as well as in Fig. 7c described below, were obtained by a combination of singular-spectrum analysis (SSA: Colebrook 1978; Broomhead and King 1986; Fraedrich 1986; Vautard and Ghil 1989) and the maximum-entropy method (MEM). This combination of two advanced spectral methods has been proven particularly effective in tens of applications to climatic and other geophysical time series; the SSA prefiltering removes, in particular, the instabilities and spurious peaks associated with MEM alone (Penland et al. 1991). The methodology and several applications are reviewed by Ghil et al. (2002b; see also the SSA-MTM Toolkit, available as freeware at <http://www.atmos.ucla.edu/tcd/>).

Of particular interest here is the peak which occurs at about 7 years. Direct comparisons between the results from these idealized double-gyre models and observed SST data of the Gulf Stream and Kuroshio axes reveal a striking similarity of spectral activities that occur in the 6–9-year interval (Speich et al. 1995). In Fig. 7b, the time evolution of the mean monthly meridional anomaly of the SST isotherm  $T = 15^\circ\text{C}$  downstream of Cape Hatteras is plotted, while its spectral signature appears in Fig. 7c. The appearance

*Fig. 7*

of the 7-year peak in the simulation (Fig. 7a) and in the observations (Fig. 7c) is indeed remarkable and far from being an isolated coincidence by now: a 7–8-yr peak has been reported in North-Atlantic SST and SLP data by Moron et al. (1998), Joyce et al. (2000), and Da Costa and Colin de Verdière (2002), while Speich et al. (1995) and Simonnet et al. (2003b) showed the presence of interannual variability of the double-gyre circulation with such a periodicity.

We attribute the 7–8-yr spectral peak reported across a hierarchy of models to the “period-doubled” gyre mode discussed at the beginning of this section: indeed, the period associated with the interannual Hopf bifurcation in these models is roughly of 3–4 years. A similar 6.5-yr peak has been found in a double-gyre simulation with a primitive equation model (Simonnet et al. 2003c). The simulation used 15 vertical levels, a horizontal grid with 14-km resolution, and a rectangular basin of 2000 km  $\times$  2000 km and a uniform depth of 5 km. The detailed results will be reported elsewhere.

To clarify further the spatial pattern of the 7-yr variability in the North Atlantic, we analyzed the United Kingdom Meteorological Office (UKMO) monthly mean SSTs from the MOHSST5 database for the century-long 1895–1994 interval. The dataset consists of anomalies relative to the 1951–1980 mean annual cycle on a  $5^\circ \times 5^\circ$  grid. In order to obtain a more homogeneous spatial and temporal coverage, we spatially averaged the data on a  $10^\circ \times 10^\circ$  grid: the SST anomaly for a  $10^\circ \times 10^\circ$  box we use is an average of four contiguous  $5^\circ \times 5^\circ$  boxes. Such an averaged box is retained if at least one of the four  $5^\circ \times 5^\circ$  boxes within it has data. We restricted the domain to the North Atlantic sector from  $85^\circ\text{W}$  to  $5^\circ\text{E}$  and  $5^\circ\text{N}$  to  $60^\circ\text{N}$  and retained only boxes that have more than 7% data coverage over the entire time interval; the number of remaining boxes is 182.

We then performed a principal component analysis on these 182 boxes and selected the first three empirical orthogonal functions (EOFs; not shown); they describe 38% of the variance and are well separated from the other EOFs. The first EOF (17 %) corresponds to an in-phase variability of the entire North Atlantic basin, with highest loadings on the subtropical gyre and south of Greenland, the second EOF (11%) represents the subpolar–

subtropical dipole, while EOF-3 (10%) is a large anomaly extending from 30°N to 60°N.

Multichannel SSA (MSSA hereafter; Plaut and Vautard 1994; Ghil et al. 2002b) reveals a robust oscillatory pair at 7–8 y, which corresponds to the mode identified by Moron et al. (1998) and by Da Costa and Colin de Verdière (2002). The phase composites of this mode’s MSSA reconstruction are plotted in Fig. 8 and reveal that the in-phase variation of the entire basin occurs mainly in phases (3, 4) and (7, 8). The phase evolution here is quite similar to that obtained by Moron et al. (1998) for their 7–8-yr mode. In our reconstruction, the subpolar gyre seems to be slightly more active during the life cycle of the oscillation than in theirs and a downstream northward propagation is apparent. The latter is reminiscent of the results of Hanson (1991) and of Sutton and Allen (1997) in the same frequency band. It is noteworthy that a similar spatio-temporal structure emerges associated with a period of 14 years (not shown here, but see Moron et al. 1998).

*Fig. 8*

The direction of propagation of SST anomalies might be a key feature in ascertaining whether the variability originates from a relaxation oscillation of the Gulf Stream or not. Simonnet and Dijkstra (2002) demonstrated that the anomalies should propagate toward the recirculation gyre that possesses stronger relative vorticity; this means northward propagation in the case where the subpolar gyre is more intense than the subtropical one. The inference above is relevant to the eastward extension of the jet, but only when the  $\mathbb{Z}_2$  symmetry is not perturbed.

In the case of the Gulf Stream, the analysis of Simonnet and Dijkstra (2002) must be modified to account for the continental geometry, as well as the spatial pattern of the climatological wind stress. It must also consider how the meandering of long oceanic jets affects the anomalies upstream, near the separation from the western boundary; see, for instance Feliks and Ghil (1996) and further references therein. To answer whether the 7–8-yr and 13–15-yr modes arise internally by mechanisms identified in this paper, its predecessors and companion papers (Dijkstra and Ghil 2005; Simonnet et al. 2005; Simonnet 2005), one needs to study how the geometry of the problem influences the distribution of the amount of relative vorticity in the recirculation gyres.

## 5. Summary and conclusions

Idealized models of the double-gyre circulation, forced by a steady wind-stress pattern, exhibit internal variability on interannual to interdecadal time scales. The internal modes so obtained provide a potential explanation for the excess energy at certain frequencies of observed variability in the mid-latitude ocean, with respect to that expected from a red-noise response to white-noise atmospheric forcing (Hasselmann 1976; Frankignoul and Hasselmann 1977; Wunsch 1999). In this regard, the organized 7–8-yr variability found in the North Atlantic SST and SLP data is of particular interest.

Clearly, to relate the observed low-frequency variability to internal modes of the wind-driven circulation, one first needs to understand in detail the transition to complex flows in the double-gyre models. The main result of this paper is the connection between the existence of multiple equilibria, the gyre-mode instabilities of the asymmetric states, and the occurrence of homoclinic bifurcations in idealized double-gyre models of the wind-driven circulation. Near the homoclinic orbits very complex flows are found; their power-spectrum exhibits a continuous component, due to their irregularity, as well as spectral peaks that rise above the continuum. These peaks are associated with relaxation oscillations produced by the gyre modes.

These relaxation oscillations arise from a three-step sequence of bifurcations that originates in the symmetry breaking, which characterizes the double-gyre problem (JJG; Speich et al. 1995; Simonnet and Dijkstra 2002; Dijkstra and Ghil 2005). We showed that these asymmetric relaxation oscillations merge into a symmetric one through a homoclinic bifurcation (Figs. 1–3) and continue to dominate the low-frequency variability of the double-gyre flows. The period of these oscillations is roughly twice that of the gyre modes that arise by Hopf bifurcation. This doubling of the period is due to the fact that the constrained symmetry of the problem tends to restore, in highly inertial and turbulent regimes, the symmetry initially broken by the pitchfork bifurcation.

The character of the homoclinic bifurcation depends on the stability properties of the

steady antisymmetric state and is either of Lorenz (1963) type or of Shilnikov (1965) type, depending on the lateral mixing strength (Figs. 4–6). This result provides also a nice connection between the successive bifurcations that occur at large values of the lateral friction in particular, the pitchfork bifurcation, to the results in Nadiga and Luce (2001) that emphasized the Shilnikov regime. However, it should be very difficult to characterize the two different types of dynamics in the observations. Moreover, we do not know yet the exact details of the transition to chaos in more complex models. Only sensitivity analysis near the bifurcation may provide definitive conclusions.

The relevance of simple double-gyre model results to observed oceanic variability was questioned at least in part, because of the use in earlier work of fairly high values of wind-stress forcing or lateral friction. Therefore, the fact that the loci of pitchfork and homoclinic bifurcations merge as both wind-stress intensity and lateral friction tend to zero (see Fig. 4) is of paramount importance. This remarkable result was also obtained analytically in a 4-mode truncated model (Fig. 3). It indicates that the bifurcations obtained in the full QG model are generic and essentially low-dimensional. Furthermore, the successive bifurcations — pitchfork, Hopf and homoclinic — are independent of the lateral mixing coefficient and may be described as an unfolding of a singularity that occurs in the reversible, Hamiltonian part of Eq. (1), with  $r_H = \sigma = 0$  (see Salmon 1988, 1998; Ghil et al. 2002a). This bifurcation tree can be understood as the evolution in phase–parameter space of a single dynamical structure. Its evolution corresponds to standard results about universal unfoldings of elementary bifurcations (see, for instance, Golubitsky and Schaeffer, 1985); the corresponding technical details will be discussed further in a companion paper by the same authors (Simonnet et al. 2005).

The unfolding in Fig. 4 seems to be rather different from the intriguing case studied by Clerc et al. (1999, 2001), although both situations can apparently lead to the same successive bifurcations. These authors showed that — for a particular class of  $\mathbb{Z}_2$ -symmetric physical systems, invariant under a time-reversal transformation and including Hamiltonian systems — the unfolding of the conservative system in the presence of terms which

break the temporal symmetry, such as viscous terms, are equivalent to the Lorenz (1963) system.

Having found this connection between the first few, local bifurcations and the highly irregular flows at very low forcing and very high Reynolds number in an equivalent-barotropic QG model for double-gyre flows in a relatively small basin is a significant theoretical step; but it is by no means a guarantee that this almost inertial dynamics will also determine the behavior in eddy-resolving ocean general circulation models. One might, for example, still question the existence of the quasi-homoclinic regimes for stratified flows in large basins under realistic wind-stress intensity. The model results so far suggest, however, that the quasi-homoclinic regime we have studied here is quite robust.

Nauw et al. (2004) have shown that homoclinic bifurcations and quasi-homoclinic regimes occur in a three-layer QG-model in a  $2000 \times 2000$  km basin. Rectification of the time-mean state can, however, stabilize the gyre modes and give rise to more exotic regimes of variability. Recent results obtained by Hogg et al. (2005) in baroclinic and turbulent simulations in an even larger,  $3840 \times 4800$  km basin show further evidence that (decadal) relaxation oscillations exist in turbulent regimes as well. How baroclinic instabilities influence the relaxation oscillations of mid-latitude oceanic jets is an area of active research, and no definitive conclusions can be reached at the present time.

Several additional steps will thus have to be taken in order to elucidate the origin of the 7–8-yr North Atlantic variability, but the evidence is mounting that it may be related to relaxation oscillations of the Gulf Stream system. These oscillations, in turn, seem to be of internal, oceanic origin and arise through gyre-mode instabilities and homoclinic bifurcations across a hierarchy of ocean models. The nonlinear theory of the wind-driven ocean's internal variability is entering a mature stage and it can claim predictive power with respect to the spatio-temporal patterns of low-frequency behavior. This theory needs therefore to be expanded to models that capture additional important processes controlling the three-dimensional ocean circulation, including stratification, bottom topography, and time-dependent wind- and buoyancy forcing.

**Acknowledgements.** This study was initiated while ES was a postdoctoral scholar at UCLA, supported under DOE Grant DE-FG02-01ER63251 to MG. He would like to thank its Department of Atmospheric and Oceanic Sciences and its Institute of Geophysics and Planetary Physics for their hospitality. ES would also like to acknowledge G. Plaut for his comments on the use of MSSA. Constructive comments from two anonymous reviewers helped improve the presentation. Numerical simulations were performed on an NCCS Cray computer (Charney) at NASA's Goddard Space Flight Center under NASA Grant NAG5-9294 and we used the ANAXV7 package of G. Plaut and R. Vautard for EOF analysis and MSSA. MG appreciates the support of NSF Grant OCE-0221066. HD is partially supported by a PIONIER grant from the Netherlands Organization for Scientific Research (NWO).

## References

- Arakawa, A. 1966. Computational design for long-term numerical integrations of the equations of atmospheric motion, *J. Comput. Phys.*, *1*, 119–143.
- Berloff, P.S., and S.P. Meacham. 1997. The dynamics of an equivalent-barotropic model of the wind-driven circulation. *J. Mar. Res.*, *55*, 407–451.
- Berloff, P.S., and J.C. McWilliams. 1999. Large-scale, low-frequency variability in wind-driven ocean gyres. *J. Phys. Oceanogr.*, *29*, 1925–1949.
- Bjerknes, J. 1964. Atlantic air-sea interactions. *Adv. Geophys.*, *10*, 1–82.
- Broomhead, D.S., and G.P. King. 1986. Extracting qualitative dynamics from experimental data. *Physica D*, *20*, 217–236, 1986.
- Bryan, K. 1963. A numerical investigation of a nonlinear model of a wind-driven ocean. *J. Atmos. Sci.*, *20*, 594–606.
- Cessi, P., and G.R. Ierley. 1995. Symmetry-breaking multiple equilibria in quasi-geostrophic wind-driven flows. *J. Phys. Oceanogr.*, *25*, 1196–1202.
- Chang, K.I., K. Ide, M. Ghil, and C.-C. A. Lai. 2001. Transition to aperiodic variability in a wind-driven double-gyre circulation model, *J. Phys. Oceanogr.*, *31*, 1260–1286.
- Chossat, P., and R. Lauterbach. 2000. *Methods in Equivariant Bifurcation and Dynamical Systems*, World Scientific, Singapore.
- Clerc, M., P. Couillet, and E. Tirapegui. 1999. Lorenz bifurcation: Instabilities in quasireversible system. *Phys. Rev. Lett.*, *83*, 3820–3823.
- Clerc, M., P. Couillet, and E. Tirapegui. 2001. The stationary instability in quasi-reversible systems and the Lorenz pendulum. *Intl. J. Bif. & Chaos*, *11*, 591–603.
- Colebrook, J.M. 1978. Continuous plankton records: zooplankton and environment, North-east Atlantic and North Sea. *Oceanol. Acta*, *1*, 9–23.
- Da Costa, E.D. and A. Colin de Verdière. 2002. The 7.7-year North Atlantic Oscillation. *Q. J. R. Meteorol. Soc.*, *128*, 797–817.
- Davis, T.A., and I.S. Duff. 1997. An unsymmetric-pattern multifrontal method for sparse LU factorization. *SIAM J. Matrix Anal. Appl.*, *18*, 140–158.

- Dettinger M. D., M. Ghil, C. M. Strong, W. Weibel, and P. Yiou. 1995. Software expedites singular-spectrum analysis of noisy time series. *Eos, Trans. AGU*, *76*, pp. 12, 14, 21.
- Dijkstra, H.A. 2000. *Nonlinear Physical Oceanography: A Dynamical Systems Approach to the Large Scale Ocean Circulation and El Niño*. Kluwer Academic Publishers, The Netherlands, 480 pp.
- Dijkstra, H.A., and C.A. Katsman. 1997. Temporal variability of the wind-driven quasi-geostrophic double gyre ocean circulation: basic bifurcation diagrams. *Geophys. Astrophys. Fluid Dyn.*, *85*, 195–232.
- Dijkstra, H.A., and M.J. Molemaker. 1999. Imperfections of the North-Atlantic wind-driven ocean circulation: Continental geometry and asymmetric windstress. *J. Mar. Res.*, *57*, 1–28.
- Dijkstra, H.A., and M. Ghil, 2005. Low-frequency variability of the large-scale ocean circulation: A dynamical systems approach. *Rev. Geophys.*, sub. judice.
- Duran, D.R. 1999. *Numerical Methods for Wave Equations in Geophysical Fluid Dynamics*. Springer-Verlag, New York, 465 pp.
- Fraedrich, K. 1986. Estimating the dimensions of weather and climate attractors. *J. Atmos. Sci.*, *43*, 419–432.
- Fofonoff, N.P. 1954. Steady flow in a frictionless homogeneous ocean. *J.Mar.Res.*, *13*, 254–262.
- Frankignoul, C., and K. Hasselmann. 1977. Stochastic climate models. II: Application to sea-surface temperature anomalies and thermocline variability. *Tellus*, *29*, 284–305.
- Ghil, M. and S. Childress. 1987. *Topics in Geophysical Fluid Dynamics: Atmospheric Dynamics, Dynamo Theory and Climate Dynamics*. Springer-Verlag, 485 pp.
- Ghil, M., Y. Feliks, and L. Sushama. 2002a. Baroclinic and barotropic aspects of the wind-driven double-gyre circulation. *Physica D*, *167*, 1–35.
- Ghil, M., R. M. Allen, M. D. Dettinger, K. Ide, D. Kondrashov, M. E. Mann, A. Robertson, A. Saunders, Y. Tian, F. Varadi, and P. Yiou. 2002b. Advanced spectral methods for climatic time series. *Rev. Geophys.*, 10.1029/2000GR000092.

- Guckenheimer, J. and P. Holmes. 1990. *Nonlinear Oscillations, Dynamical Systems and Bifurcations of Vector Fields*, 2nd ed., Springer-Verlag, 453 pp.
- Glendinning, P. 1984. Bifurcations near homoclinic orbits with symmetry. *Phys. Lett.*, *103A*, 163–166.
- Golubitsky, M. and D.G. Schaeffer, 1985: *Singularities and Groups in Bifurcation Theory, part I*. Springer Verlag, New-York, 488 pp.
- Hanson, H.P. 1991. Climatological perspectives, oceanographic and meteorological, on variability in the subtropical convergence zone in the Northwestern Atlantic. *J. Geophys. Res.*, *96*, 8517–8529.
- Hasselmann, K. 1976. Stochastic climate models. I: Theory. *Tellus*, *28*, 473–485.
- McC Hogg, A., P.D. Killworth, J.R. Blundell, and W.K. Dewar. 2005. On the mechanisms of decadal variability of the wind-driven ocean circulation. *J. Phys. Oceanogr.*, *in press*.
- Jiang, S., F.-F. Jin, and M. Ghil. 1993. The nonlinear behavior of western boundary currents in a wind-driven, double-gyre, shallow-water model. Ninth Conf. Atmos. & Oceanic Waves and Stability (San Antonio, TX), American Meteorological Society, Boston, Mass., pp. 64–67.
- Jiang, S., F.F. Jin, and M. Ghil. 1995. Multiple equilibria, periodic, and aperiodic solutions in a wind-driven, double-gyre, shallow-water model. *J. Phys. Oceanogr.*, *25*, 764–786.
- Joyce, T.M., Deser C. and M. Spall. 2000. The relation between decadal variability of subtropical mode water and the North Atlantic Oscillation. *J. Clim.*, *13*, 2550–2569.
- Keller, H.B. 1977. Numerical solution of bifurcation and nonlinear eigenvalue problems. in *Applications of Bifurcation Theory*, pp. 359–384, (ed. P.H. Rabinowitz), Academic Press.
- Keppenne, C. L., and M. Ghil. 1993. Adaptive filtering and prediction of noisy multivariate signals: An application to subannual variability in atmospheric angular momentum. *Intl. J. Bifurcation & Chaos*, *3*, 625–634.
- Kimoto, M., and M. Ghil. 1993a. Multiple flow regimes in the Northern Hemisphere winter. Part I: Methodology and hemispheric regimes. *J. Atmos. Sci.*, *50*, 2625–2643.

- Kimoto, M., and M. Ghil. 1993b. Multiple flow regimes in the Northern Hemisphere winter. Part II: Sectorial regimes and preferred transitions. *J. Atmos. Sci.*, *50*, 2645–2673.
- Kubiček, M., and M. Marek. 1983. *Computational Methods in Bifurcation Theory and Dissipative Structures*. Springer-Verlag, 243 pp.
- Kuznetsov, Y.A. 1995. *Elements of Applied Bifurcation Theory*, Springer-Verlag, 623 pp.
- Legras, B., and M. Ghil. 1985. Persistent anomalies, blocking and variations in atmospheric predictability, *J. Atmos. Sci.*, *42*, 433–471.
- Lorenz, E.N. 1963. Deterministic non-periodic flow. *J. Atmos. Sci.*, *20*, 130–141.
- McCalpin, J., and D. Haidvogel. 1996. Phenomenology of the low-frequency variability in a reduced-gravity, quasi-geostrophic double-gyre model. *J. Phys. Oceanogr.*, *26*, 739–752.
- Meacham, S.P. 2000. Low-frequency variability in the wind-driven circulation. *J. Phys. Oceanogr.*, *30*, 269–293.
- Mizuno, K., and W.B. White. 1983. Annual and interannual variability in the Kuroshio current system. *J. Phys. Oceanogr.*, *20*, 1349–1378.
- Moron, V., R. Vautard, and M. Ghil. 1998. Trends, interdecadal and interannual oscillations in global sea-surface temperatures. *Clim. Dyn.*, *14*, 545–569.
- Munk, W. 1950. On the wind-driven ocean circulation. *J. Meteorology*, *7*, 79–93.
- Nadiga, B.T., and Luce, B.P. 2001. Global bifurcation of Shilnikov type in a double-gyre ocean model. *J. Phys. Oceanogr.*, *31*, 2669–2690.
- Nauw, J.J. and H.A. Dijkstra. 2001. The origin of low-frequency variability of double-gyre wind-driven flows. *J. Mar. Res.*, *59*, 567–597.
- Nauw, J.J., H.A. Dijkstra, and E. Simonnet. 2004. Regimes of low-frequency variability in a three-layer quasi-geostrophic ocean model. *J. Mar. Res.*, *62*, 684–719.
- Penland, C., M. Ghil and K. M. Weickmann, 1991: Adaptive filtering and maximum entropy spectra, with application to changes in atmospheric angular momentum. *J. Geophys. Res.*, *96*, 22, 659–22, 671.
- Plaut, G. and R. Vautard. 1994. Spells of low-frequency oscillations and weather regimes in the northern hemisphere. *J. Atmos. Sci.*, *51*, 210–236.

- Plaut, G., M. Ghil, and R. Vautard. 1995. Interannual and interdecadal variability in 335 Years of Central England temperatures. *Science*, *268*, 710–713.
- Primeau, F. W. 1998. Multiple equilibria of a double-gyre ocean model with super-slip boundary conditions. *J. Phys. Oceanogr.*, *28*, 2130–2147.
- Primeau, F. W. 2002. Multiple equilibria and low-frequency variability of the wind-driven ocean circulation. *J. Phys. Oceanogr.*, *32*, 2236–2256.
- Qiu, B., and T.M. Joyce. 1992. Interannual variability in the mid- and low-latitude western North Pacific. *J. Phys. Oceanogr.*, *22*, 1062–1079.
- Ruelle, D., and F. Takens. 1971. On the nature of turbulence. *Commun. Math. Phys.*, *20*, 167–192.
- Salmon, R. 1988. Hamiltonian fluid mechanics. *Annu. Rev. Fluid Mech.*, *20*, 225–256.
- Salmon, R. 1998. *Lectures on Geophysical Fluid Dynamics*. Oxford Univ. Press, 378 pp.
- Schmeits M.J. and H.A. Dijkstra. 2001. Bimodality of the Gulf Stream and Kuroshio. *J. Phys. Oceanogr.*, *31*, 3435–3456.
- Sheremet, V.A., G.R. Ierley, and V.M. Kamenkovitch. 1997. Eigenanalysis of the two-dimensional wind-driven ocean circulation problem. *J. Mar. Res.*, *55*, 57–92.
- Shilnikov, L. P. 1965. A case of the existence of a denumerable set of periodic motions. *Sov. Math. Dokl.*, *6*, 163–166.
- Simonnet, E. 1998. *Some Numerical Problems Related to Geophysical Flows*. Ph.D.thesis, Paris-Sud University, 154 pp.
- Simonnet E., R. Temam, S. Wang, M. Ghil, and K. Ide. 1998. Successive bifurcations in a shallow-water ocean model. In *16th Intl. Conf. Numerical Methods Fluid Dynamics, Lecture Notes in Physics*, *515*, Springer-Verlag, 225–230.
- Simonnet, E. and H.A. Dijkstra. 2002. Spontaneous generation of low-frequency modes of variability in the wind-driven ocean circulation. *J. Phys. Oceanogr.*, *32*, 1747–1762.
- Simonnet, E., M. Ghil, K. Ide, R. Temam, and S. Wang. 2003a. Low-frequency variability in shallow-water models of the wind-driven ocean circulation. Part I: Steady-state solutions. *J. Phys. Oceanogr.*, *33*, 712–728.

- Simonnet, E., M. Ghil, K. Ide, R. Temam, and S. Wang. 2003b. Low-frequency variability in shallow-water models of the wind-driven ocean circulation. Part II: Time-dependent solutions. *J. Phys. Oceanogr.*, *33*, 729–752.
- Simonnet, E., T. Tachim Medjo and R. Temam, 2003c: Barotropic-Baroclinic formulation of the primitive equations of the ocean. *Appl. Analysis*, **82**, 439–456.
- Simonnet, E. 2005. Quantization of the low-frequency variability of the double-gyre circulation. *J. Phys. Oceanogr.*, *sub judice*.
- Simonnet, E., M. Ghil, and H.A. Dijkstra. 2005. Quasi-homoclinic behavior of the barotropic quasi-geostrophic double-gyre circulation. *Chaos*, *to be submitted*.
- Sparrow, C.T. 1983. *Lorenz Equations: Bifurcations, Chaos, and Strange Attractors*. Springer-Verlag.
- Speich, S., H.A. Dijkstra, and M. Ghil. 1995. Successive bifurcations in a shallow-water model applied to the wind-driven ocean circulation. *Nonlin. Proc. Geophys.*, *2*, 241–268.
- Stewart, W.J., and A. Jennings. 1981. A simultaneous iteration algorithm for real matrices. *ACM Trans. Math. Software*, *7*, 184–198.
- Stommel, H. 1948. The westward intensification of wind-driven ocean currents. *Trans. Amer. Geophys. Union*, *29*, 202–206.
- Sutton, R.T., and M.R. Allen. 1997. Decadal predictability in North Atlantic sea surface temperature and climate. *Nature*, *388*, 563–567.
- Taft, B.A. 1972. Characteristics of the flow of the Kuroshio south of Japan. In *Kuroshio—Its Physical Aspects*, H. Stommel and K. Yoshida, Eds., University of Tokyo Press, 165–216.
- Vautard, R., and M. Ghil. 1989. Singular spectrum analysis in nonlinear dynamics, with applications to paleoclimatic time series. *Physica D* *35*, 395–424.
- Veronis, G. 1963. An analysis of wind-driven ocean circulation with a limited number of Fourier components. *J. Atmos. Sci.*, *20*, 577–593.
- Veronis, G. 1966. Wind-driven ocean circulation. II: Numerical solution of the nonlinear problem. *Deep Sea Research*, *13*, 31–55.
- Wiggins, S. 1987. *Global Bifurcations and Chaos: Analytical Methods*. Springer-Verlag, 494

pp.

Wunsch, C. 1999. The interpretation of short climate records, with comments on the North Atlantic and Southern Oscillations. *Bull. Amer. Met. Soc.*, *80(2)*, 245–255.

Yoshida, K. 1961. On the variation of Kuroshio and cold water mass off Enshu Nada (In Japanese with English abstract). *Hydrogr. Bull.*, *67*, 54–57.

---

*E. Simonnet, Institut Non-Linéaire de Nice (INLN),*

*UMR 6618, CNRS,*

*M. Ghil, Département Terre-Atmosphère-Océan and Laboratoire de Météorologie Dynamique*

*Ecole Normale Supérieure, 24, rue Lhomond*

*F-75231 Paris Cedex 05, France*

*and*

*Department of Atmospheric and Oceanic Sciences and*

*Institute of Geophysics and Planetary Physics, UCLA,*

*Los Angeles, CA 90095-1565, USA*

*H.A. Dijkstra, Institute for Marine and Atmospheric Research Utrecht (IMAU)*

*Department of Physics and Astronomy, Utrecht University,*

*Utrecht, the Netherlands*

*and*

*Department of Atmospheric Science,*

*Colorado State University, Fort Collins, CO, 80523-1371*

*(Received )*

Table 1. Reference values of parameters in the equivalent-barotropic QG model.

Parameter	Value	Parameter	Value
Dimensional			
$U$	$1 \text{ ms}^{-1}$	$L = R_d$	$50 \cdot 10^3 \text{ m}$
$g'$	$0.025 \text{ ms}^{-2}$	$f_0$	$10^{-4} \text{ s}^{-1}$
$L/U$	$13.8 \text{ h} = 49680 \text{ s}$	$\beta_0$	$1.6 \cdot 10^{-11} \text{ m}^{-1}\text{s}^{-1}$
$D$	$1000 \text{ m}$	$A_H$	$150 \text{ m}^2\text{s}^{-1}$
Dimensionless			
$\beta$	$0.04$	$r_H$	$3 \cdot 10^{-3}$
$\delta_I$	$5$	$\delta_M$	$0.421$

Table 2. Reference values of the model's nondimensional coefficients for  $s = 2$ .

$c_1$	$c_2$	$c_3$	$c_4$	$c_5$	$c_6$
0.35	0.19	0.11	0.23	0.39	0.35

## Figure Captions

**Figure 1:** Schematic bifurcation diagram of an equivalent-barotropic QG model, plotted in terms of an asymmetry measure  $\Delta_E$  (see section 3a further below) vs. wind-stress intensity. The limit cycles are schematically drawn for illustrative purpose and the stream-function patterns corresponding to the three steady-state branches — subtropical, anti-symmetric, and subpolar (from top to bottom) — are indicated in the right panels. The values of  $\psi_{\max}$  in the latter indicate the maximum value of  $\psi$  located in the subtropical gyre.

**Figure 2:** Unfolding of the relaxation oscillations induced by the gyre modes, shown in the plane spanned by the total potential energy of the solution  $E_p$  and the difference  $\Delta_E$  between the subpolar potential energy and the subtropical one (see text for details). The orbits of several limit cycles are plotted for  $A_H = 300 \text{ m}^2\text{s}^{-1}$  and, in order of increasing amplitude: (a)  $\sigma = 0.29623 \cdot 10^{-3}$ , (b)  $\sigma = 0.2965 \cdot 10^{-3}$ , (c)  $\sigma = 0.2980 \cdot 10^{-3}$ , and (d)  $\sigma = 0.2992 \cdot 10^{-3}$ ; the corresponding periods are 2.07 y, 3.04 y, 3.30 y and  $\simeq 8.3$  y (weakly aperiodic), respectively. For clarity, only the orbits looping around the subpolar branch ( $\Delta_E > 0$ ) are shown; the motion along each orbit goes outward from the point (0, 3.8) slowly, to return rapidly toward and along the axis  $\Delta_E = 0$ .

**Figure 3:** Bifurcation diagram of the highly truncated, four-mode model (5), projected onto the  $(A_1 + A_3, A_2)$  plane for  $\mu = 1$  and  $s = 2$ ;  $P$  stands for pitchfork bifurcation at  $\sigma = \sigma_P = 7.61$ , while  $\sigma = \sigma_{hc} \simeq 10.4299$  at the homoclinic bifurcation. The branches of periodic orbits are replaced by several explicitly computed limit cycles.

**Figure 4:** Regime diagram of the full model (1), showing the loci of pitchfork (light solid curve), homoclinic (heavy solid curve) and saddle-node bifurcations (dash-dotted curve) in the 2-parameter plane spanned by the nondimensional viscosity  $r_H$  and wind-

stress intensity  $\sigma$ . The corresponding values of the dimensional viscosity  $A_H$  range from 20 to 300  $\text{m}^2\text{s}^{-1}$ . The filled circle marks the transition between Lorenz chaos and Shilnikov chaos (see text for details).

**Figure 5:** Schematic diagram of the two types of homoclinic orbits: (a) Lorenz type; and (b) Shilnikov type.

**Figure 6:** Leading instabilities that occur along the homoclinic locus of Fig. 4, as a function of the viscosity  $r_H$ . The curves plotted in the large panel are the real parts of the leading eigenvalues (the ones closest to the imaginary axis) at the value of  $r_H$  on the abscissa, while the corresponding value of  $\sigma$  is the one read off the heavy solid curve in Fig. 4. The spatial patterns of the associated streamfunction fields (real for the P- and L-mode and complex conjugate for the Rossby basin mode) are plotted in the adjacent small panels and connected by arrows to the appropriate curves in the main panel.

**Figure 7:** Comparison between low-frequency variability in an idealized double-gyre model and in observations of the Gulf Stream axis. (a) Spectral results for a 2.5-layer SW model for a basin that approximates the North Atlantic in size and shape, using an idealized wind stress. Maximum entropy (MEM) spectrum of the subpolar-gyre kinetic energy; the window length used for the SSA prefiltering is 20 years, the number of reconstructed components retained is 12, and the MEM order is 40; after Simonnet et al. (2003b). (b) Time evolution of the monthly-mean meridional anomaly of the position of the SST isotherm  $T = 15^\circ$ , calculated in km with respect to  $41^\circ$  N of latitude, at  $50^\circ$  W, from January 1960 to December 1997. The SST field is based on the Cooperative Ocean Atmosphere Data Set (COADS) and it has been spatially interpolated by cubic splines in the interval  $30^\circ\text{N}$ – $60^\circ\text{N}$  in order to compute the deviation from its mean-latitude position. The SSA reconstruction (heavy red line) is superimposed on the original time series (light black line); it has been obtained by filtering out the seasonal cycle and retaining the 8

lowest-frequency EOFs, for an SSA window of 16 years. (c) Maximum-entropy spectrum of the heavy red line in Fig. 7b; the order of the MEM is 40. Both the spectrum of the model simulation (panel a) and of the observed data (panel c) are in log-linear coordinates.

**Figure 8:** Phase composites of the reconstructed 7–8-yr SST oscillation. The MSSA window length is 40 yr and the contour interval is  $0.02^\circ$  C.

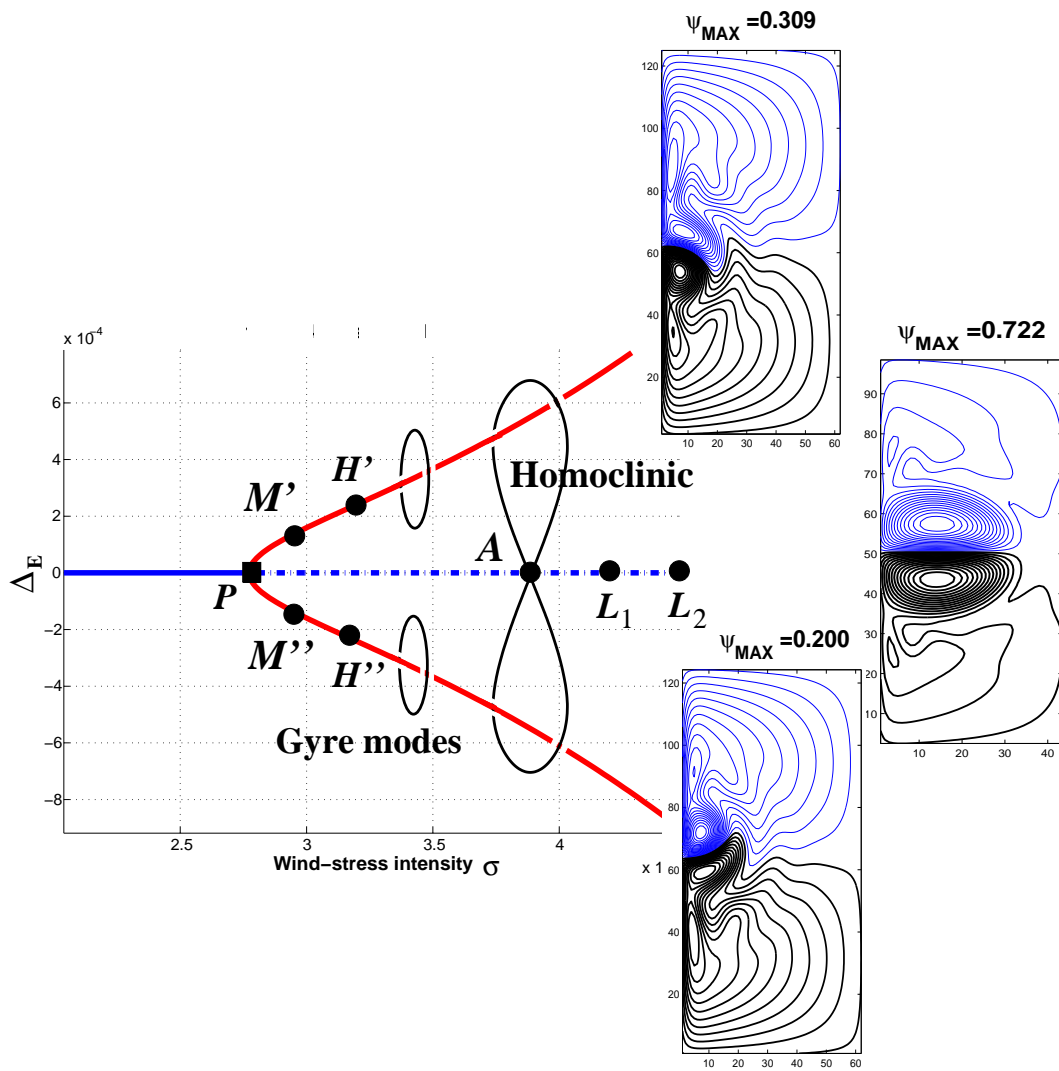


Figure 1:

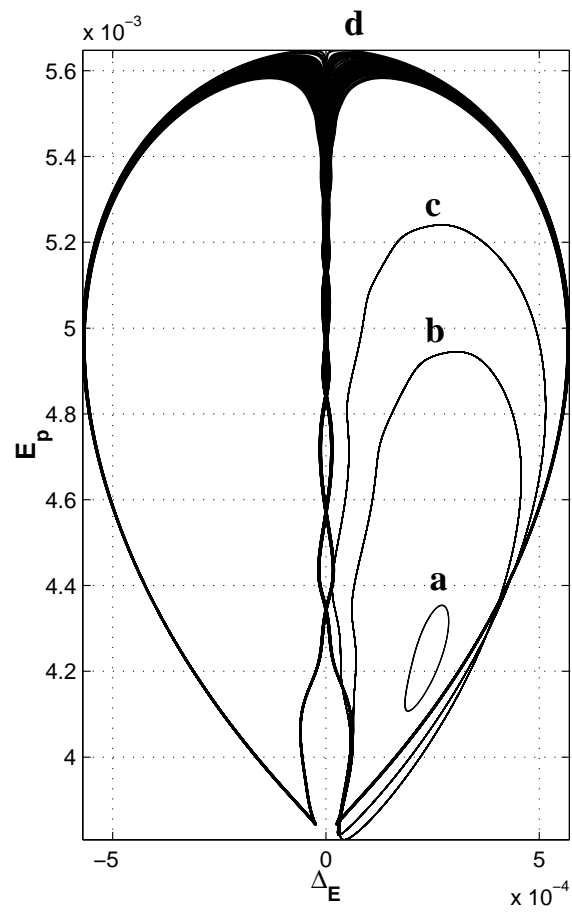


Figure 2:

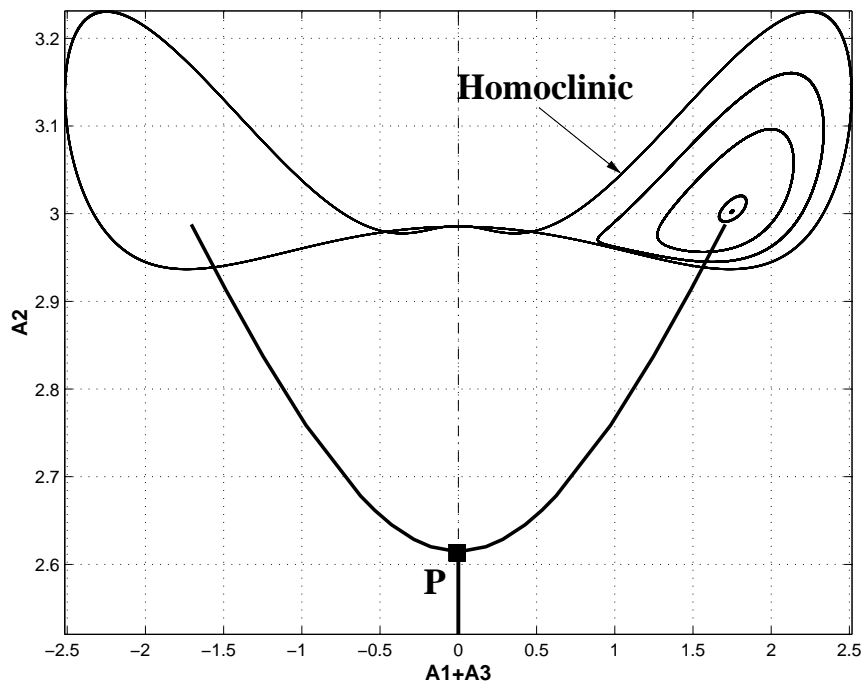


Figure 3:

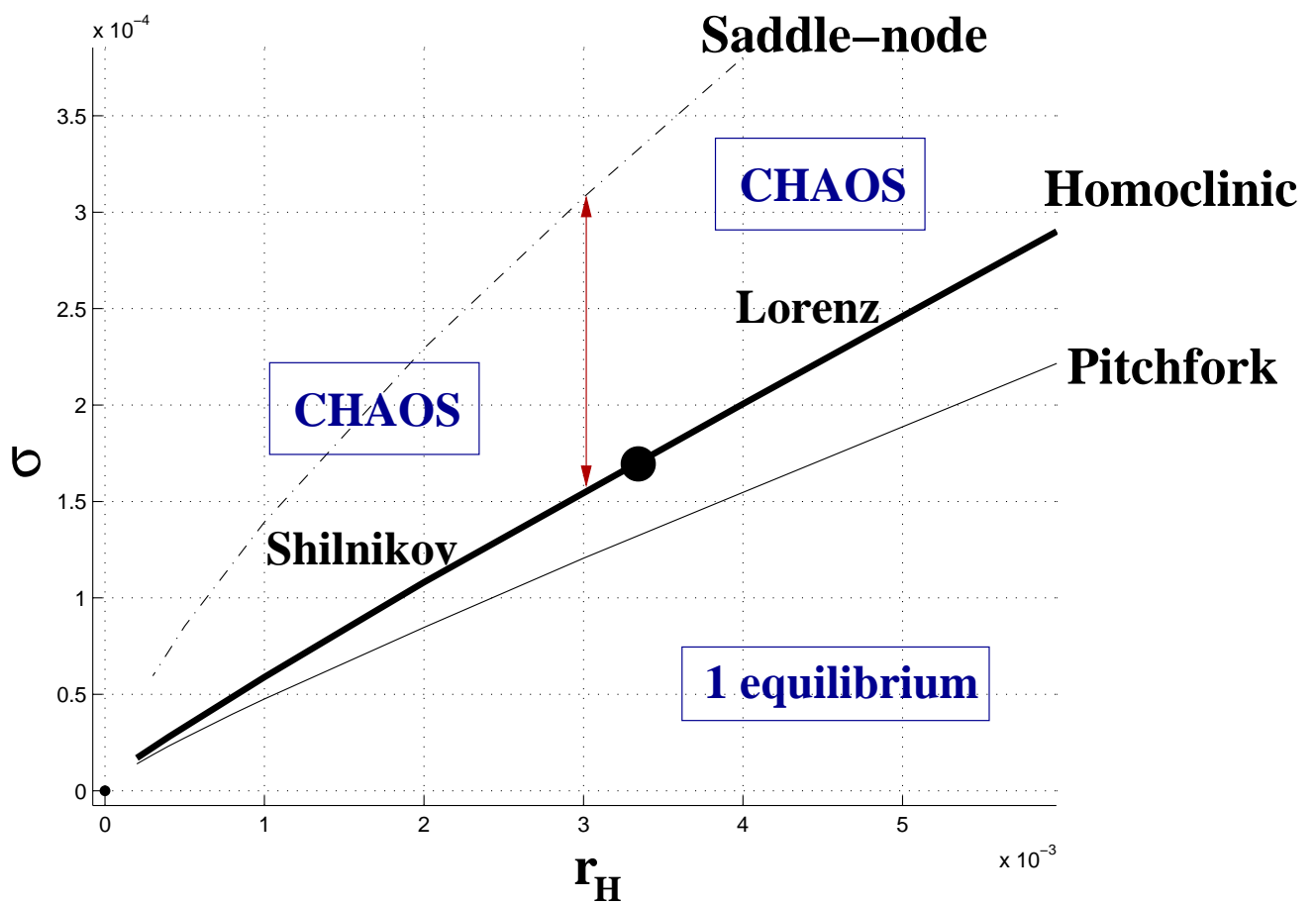
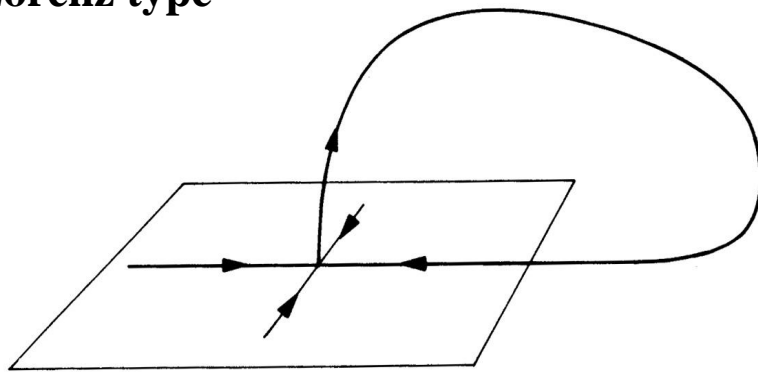


Figure 4:

**a) Lorenz type**



**b) Shilnikov type**

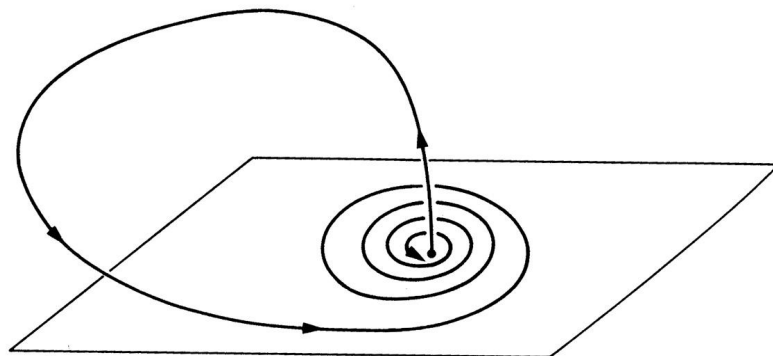


Figure 5:

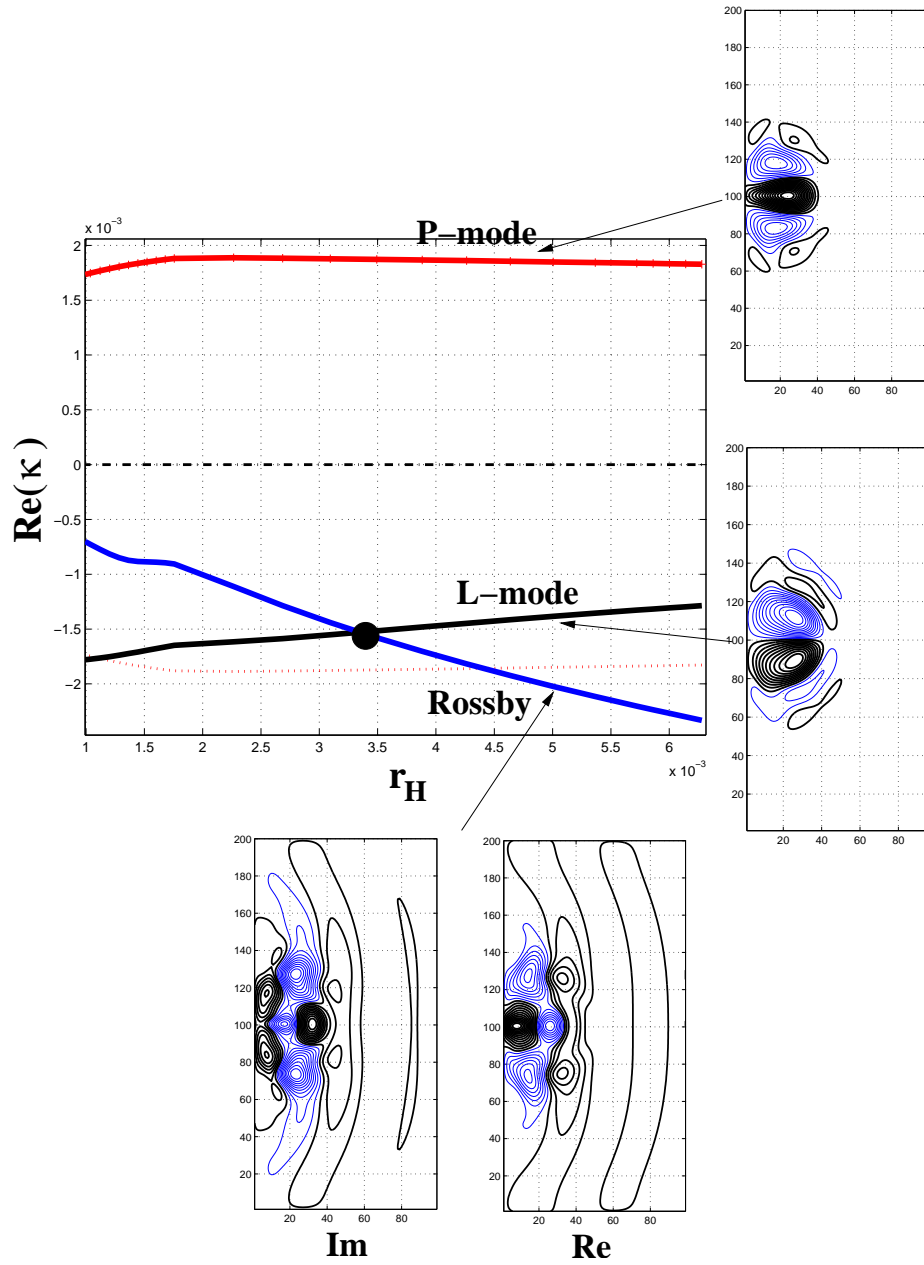


Figure 6:

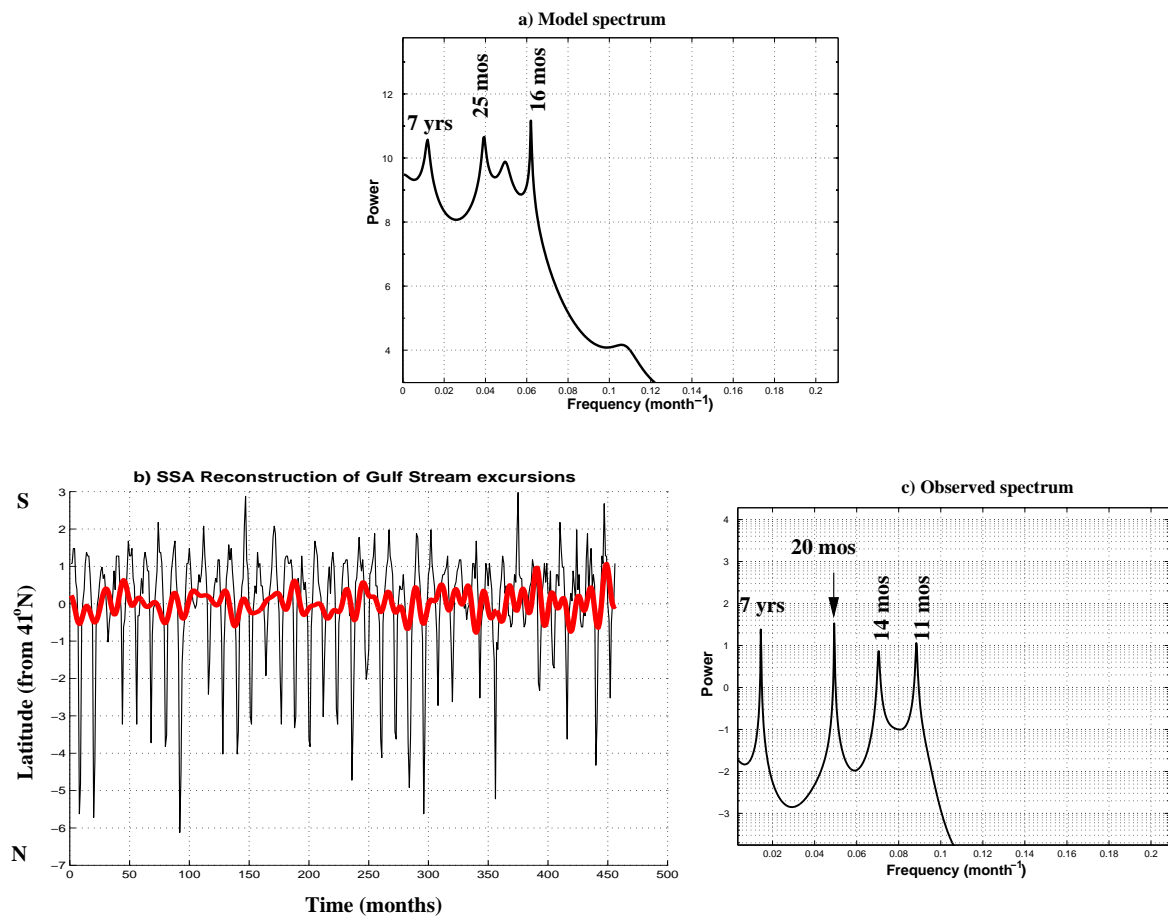


Figure 7:

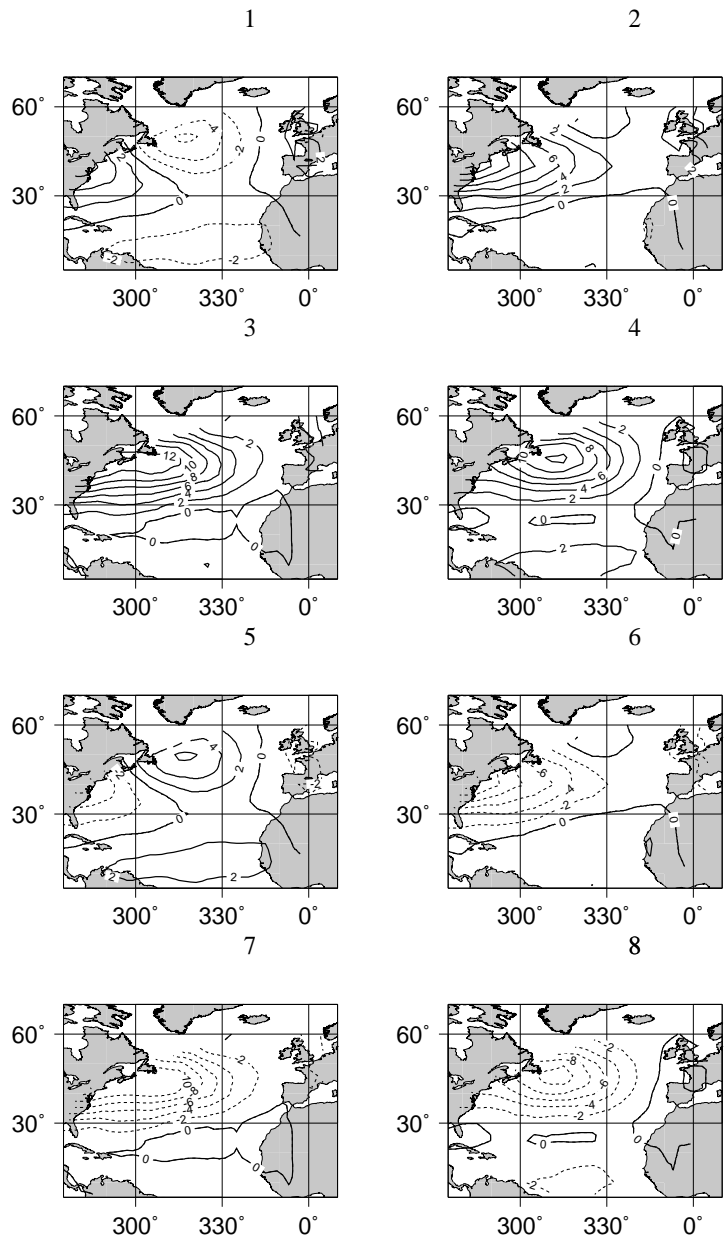


Figure 8: